UC Santa Barbara
UC Santa Barbara Previously Published Works

Title
Design Principles for Enhancing Photoluminescence Quantum Yield in Hybrid Manganese Bromides

Authors
Mao, Lingling
Guo, Peijun
Wang, Shuxin
et al.

Peer reviewed

Design Principles for Enhancing Photoluminescence Quantum Yield in Hybrid Manganese Bromides

Lingling Mao[1], Peijun Guo[3,4], Shuxin Wang[1], Anthony K. Cheetham[1,5]* and Ram Seshadri[1,2]*

[1]Materials Research Laboratory and Materials Department, [2]Department of Chemistry and Biochemistry, University of California, Santa Barbara, California 93106, United States

[3]Center for Nanoscale Materials, Argonne National Laboratory, 9700 South Cass Avenue, Lemont, Illinois 60439, United States

[4]Department of Chemical and Environmental Engineering, Yale University, 9 Hillhouse Avenue, New Haven, CT 06520, United States

[5]Department of Materials Science & Engineering, National University of Singapore 9 Engineering Drive 1, Singapore 117576, Singapore

ABSTRACT: Hybrid manganese halides have attracted widespread attention on account of their highly emissive optical properties. To understand the underlying structural factors that dictate the photoluminescence quantum yield (PLQY) of these materials, we report five new hybrid manganese bromides with the general formula $A_m MnBr_4$ [$m = 1$ or 2, A = dimethylammonium (DMA), 3-methylpiperidinium (3-MP), 3-aminometylpiperidinium (3AMP), heptamethylenimine (HEP) and trimethylphenylammonium (TMPEA)]. By studying the crystal structures and optical properties of these materials and combining our results with the findings from previously reported analogs, we have found a direct correlation between Mn⋯Mn distance and the PLQY, where high PLQYs are associated with long Mn⋯Mn distances. This effect can be viewed as a manifestation of the concentration-quenching effect, except these are in stoichiometric compounds with precise interatomic distances, rather than random alloys. To gain better separation of the Mn centers and prevent energy transfer, a bulky singly-protonated cation that avoids H-bonding is ideal. We have demonstrated this principle in one of our newly reported material, $(TMPEA)_2MnBr_4$, where a PLQYs of 70.8 % for a powder sample and 98 % for a large single crystal sample is achieved. Our study reveals a generalized method for improving PLQYs in hybrid manganese bromides and is readily extended to designing all varieties of highly emissive hybrid materials.

INTRODUCTION

Hybrid metal halide materials possess a wide range of interesting properties that can be tuned by varying the organic and inorganic components.[1-3] For example, the organic-inorganic perovskite halides demonstrate exceptional optoelectronic performance in solar cells,[4,5] light-emitting diodes,[6,7] lasers,[8,9] and detectors.[10-13] With different metal halide combinations, the structural motifs can vary from highly extended structures to lower dimensional structures.[14-16] In the cases of transition metal halides, isolated octahedra or tetrahedra are often observed. Examples include Mn-,[17] Ru-,[18] Co-,[19] Cu-based[20] systems, which exhibit interesting magnetic, dielectric and optical properties.[21-23]

Hybrid manganese halides are of particular interests for light-emission related applications[24,25] due to their high photoluminescence quantum yields (PLQYs). Mn has also been widely used as a dopant,[26-29] and is known to effectively give rise to or enhance the PLQY of the host system.[30,31] The emission color of Mn^{II} is highly dependent on the coordination environment of the metal; when it is octahedrally coordinated the emission color is red,[32,33] whereas when it is tetrahedrally coordinated the emission color is green.[17] The intense green emission originates from the absence of an inversion center in the asymmetric T_d environment and the small crystal field splitting energy of $[MnX_4]^{2-}$ (where X is the halogen) which increase the electric-dipole oscillator strength.[34] Dual color emission also exists when both coordination environments are present.[35,36] Tribolu-
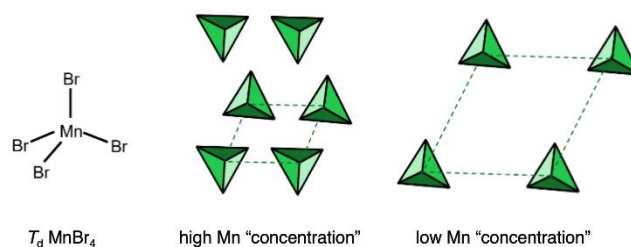

Figure 1. Schematic illustration of manganese bromide in tetrahedral environment with short Mn⋯Mn distances (high Mn "concentration") vs. long Mn⋯Mn distances (low Mn "concentration").

minescence[37,38] has been observed in noncentrosymmetric crystals and pressure-induced photoluminescence was previously studied[34,39] in hybrid manganese halide systems. Extensive literature demonstrating high PLQYs has been reported on these materials,[24,40-48] but there has not been clear discussion of why certain compounds have better emission efficiencies. Oftentimes, only materials with high PLQYs are reported, leaving out the materials with low PLQYs, which impacts the ability to establish structure-property relations.
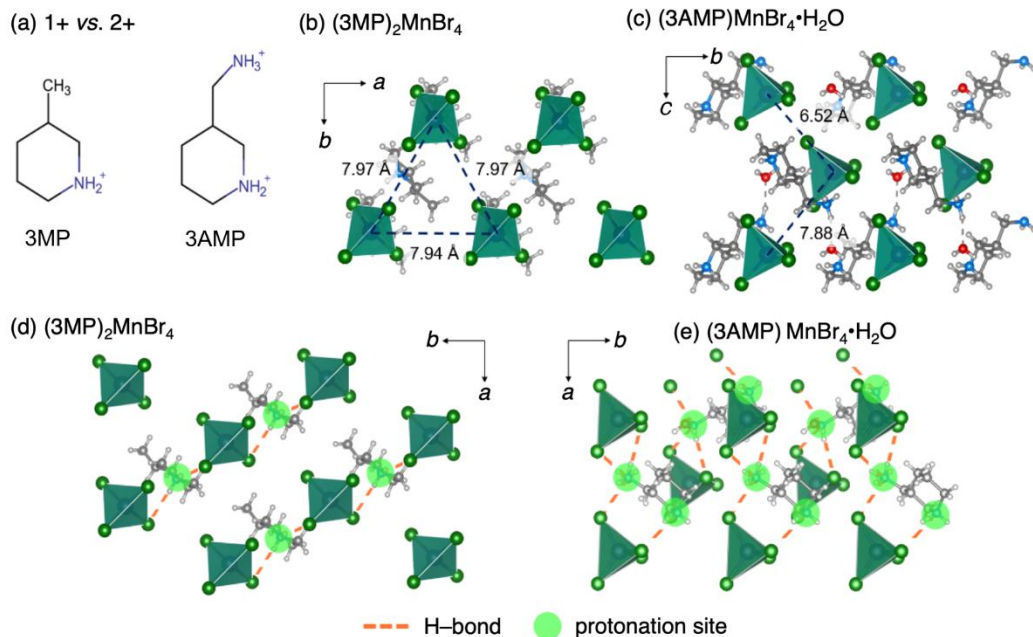
Figure 2. (a) Organic *A* cations 3-methylpiperidinium (3-MP, left) and 3-aminometylpiperidinium (3AMP, right). (b) Crystal structure of (3MP)$_2$MnBr$_4$, with blue dashes indicating the closest neighboring Mn⋯Mn distances (7.94 Å and 7.97 Å). (c) Crystal structure of (3AMP)MnBr$_4$, with blue dashes indicating the closest neighboring Mn⋯Mn distances (6.52 Å and 7.88 Å). In (d) and (e) the protonation sites in (3MP)$_2$MnBr$_4$ and (3AMP)MnBr$_4$ are highlighted in green and H-bonding interactions labeled with orange dashes. The 2+ cation template structure (3AMP)MnBr$_4$ shows significantly more H-bonding interactions (H-bond cut-off: 3.5 Å).

Here, we demonstrate key structure-PLQY correlations by studying new and reported A_mMnBr$_4$ (m = 1 or 2) materials that emit green light (with Mn adopting T_d geometry, Figure 1). In a doped system, there is usually a limit for the dopant level due to concentration quenching. However, in a non-doped system that solely consists of organic cations and [MnBr$_4$]$^{2-}$ anions, the positions of the Mn centers are fixed by the crystal structure. In stoichiometric laser materials such as NdP$_3$O$_9$ and NdP$_5$O$_{14}$, the shortest Nd⋯Nd distances are 4.2 and 5.2 Å.[49] By carefully varying the organic cation in such systems, we have managed to expand the shortest Mn⋯Mn distances ranging from 6.2 Å to 9.0 Å. We combine our results with previous literature reports and identify a trend whereby the PLQY proportionally increases as the average Mn⋯Mn distance within the crystal structure increases. A threshold of ~9 Å of Mn separation has shown optimal performances. This can be viewed as an effect that is similar to concentration quenching. Short Mn⋯Mn distances can be viewed as high Mn concentration and vice versa (Figure 1). Our results show that in order to achieve high PLQY in these systems, a bulky, rigid, singly protonated cation is ideal. To minimize H-bonding interactions that potentially decrease the Mn⋯Mn distance, steric hindrance on the protonation site is also preferred. Our work highlights the structure-property relations in this widely studied family and provides design rules for future endeavors in light-emitting materials

RESULTS AND DISCUSSION

Crystal structures and the Mn⋯Mn distances. A series of organic cations were employed to form the hybrid manganese bromides. We have grouped them based on the contrast or similarity in the following order: (i) 1+ vs. 2+ cations; (i) small vs. large cations; (i) cations with similar functional groups.

(i) 1+ vs 2+ cations. The first group of direct comparison comes from (3MP)$_2$MnBr$_4$ and (3AMP)MnBr$_4$ (3MP = 3-

methylpiperidinium, 3AMP = 3-aminomethylpiperidinium), as seen in Figure 2. (3MP)$_2$MnBr$_4$ and (3AMP)MnBr$_4$ crystallize in the monoclinic space groups $C2/m$ and $P2_1$, respectively. Detailed crystallographic refinement details are given in Table S1. To charge balance the A_mMnBr$_4$ system, it is natural that when m = 2 (1+ cation) it should require more *A* cations than in the m = 1 (2+ cation) case, thus potentially pushing the MnBr$_4^{2-}$ tetrahedra further apart. This is reflected in Figures 2(b) and (c), where the closest Mn⋯Mn distances for (3MP)$_2$MnBr$_4$ are 7.94 Å and 7.97 Å. On the other hand, with one more protonated ammonium group, the chance of the 2+ cation interacting with Br will further increase. It is clear that for (3AMP)MnBr$_4$, the extra NH$_3^+$ group of 3AMP causes more hydrogen bonding interactions, as seen in Figures 2(d) and (e). As a consequence, the Mn⋯Mn distances are closer in (3AMP)MnBr$_4$ (6.52 Å and 7.88 Å).

(ii) Small vs. large cations. A significant increase in the separation of the MnBr$_4^{2-}$ tetrahedral will occur when using a large, bulky cation such as tetraphenylphosphonium (PPh$_4^+$). The structure of (PPh$_4$)$_2$MnBr$_4$ was previously reported by Xu *et al.* and the material was used in organic light-emitting diodes.[24] Here, we use dimethylammonium (DMA), one of the smallest ammonium cation, to compare its templating effect with PPh$_4^+$ in the A_2MnBr$_4$ system. Due to the small size of DMA, the resulting Mn⋯Mn distances are very short (6.22 Å and 6.85 Å). With a much larger size and the steric hindrance of four aromatic rings attached on each cation, in (PPh$_4$)$_2$MnBr$_4$, the Mn⋯Mn distances (10.37 Å and 11.38 Å) are almost twice those in (DMA)$_2$MnBr$_4$.
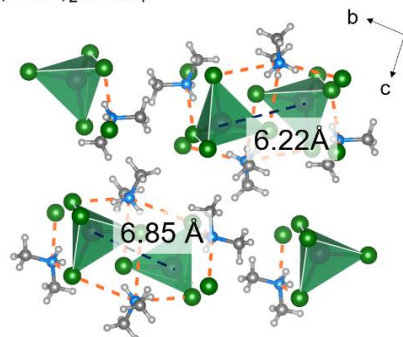
(iii) Cations with similar functional groups. From the above examples of (3AMP)MnBr$_4$ and (DMA)$_2$MnBr$_4$, it is evident that the H-bonding interactions bring MnBr$_4^{2-}$ tetrahedra closer together. In the cases of (TMPEA)$_2$MnBr$_4$ and
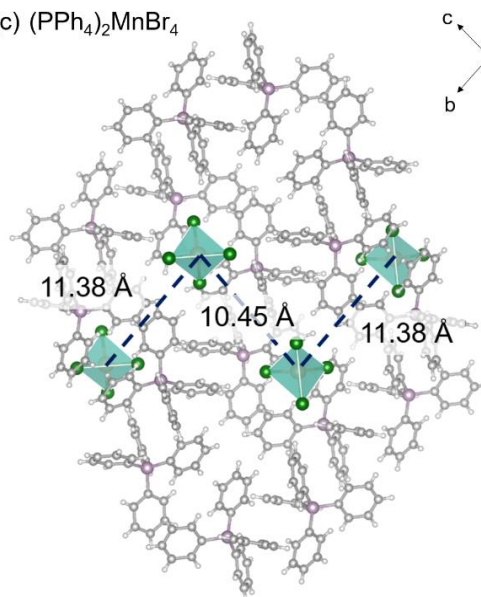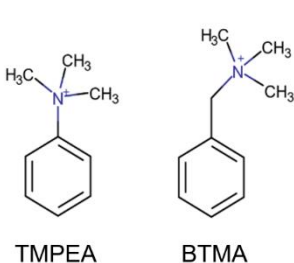
(BTMA)$_2$MnBr$_4$ (TMPEA = trimethylphenylammonium,
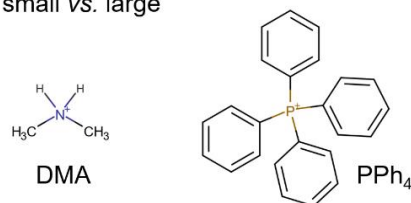
Figure 3. (a) Organic *A* cation dimethylammonium (DMA, left) and tetraphenylphosphonium (PPh$_4^+$), right. (b) Crystal structure of (DMA)$_2$MnBr$_4$; orange dashes show the H-bonding interactions; shortest Mn···Mn distances (6.22 Å and 6.85 Å) labeled with blue dashes. (c) Crystal structure of (PPh$_4$)$_2$MnBr$_4$, redrawn from ref. 24. The shortest Mn···Mn distances are 10.45 Å and 11.38 Å.

BTMA = benzyltrimethylammonium), with more substitution on the cation site [N(CH$_3$)$_3$]$^+$ and the rigid ar2omatic rings [Figure 4(a)], considerable Mn···Mn separation can be achieved. (TMPEA)$_2$MnBr$_4$ crystallizes in the monoclinic space group *C*2/*c*. The unique packing of the TMPEA cations and MnBr$_4^{2-}$ tetrahedra leads to an enlarged unit cell comprising 3 units of (TMPEA)$_2$MnBr$_4$ (formula = (C$_9$NH$_{14}$)$_6$Mn$_3$Br$_{12}$). (BTMA)$_2$MnBr$_4$ was previously reported by Cai *et al.*, with a high PLQY of 72%.[41] In these two examples, there is no H-bonding. The steric effect of the rigid aromatic ring also helps to push the [MnBr$_4$]$^{2-}$ tetrahedra further apart, resulting in longer Mn···Mn distances (8.64 Å and 9.58 Å for (TMPEA)$_2$MnBr$_4$; 8.97 Å and 9.58 Å for (BTMA)$_2$MnBr$_4$). With an extra -CH2- group in the longer cation, the shortest Mn···Mn distance for (BTMA)$_2$MnBr$_4$ is slightly longer than that in (TMPEA)$_2$MnBr$_4$. The correlation between Mn···Mn distances and PLQY will be discussed in the next section.

Correlation between Mn···Mn distances and PLQY. In inorganic phosphors, fluorescence activator ions such as Mn^{2+}, Dy^{3+}, and Er^{3+}, and are often used as dopants. In doped systems, nonradiative relaxation process can be reduced by keeping the dopant level low, thereby optimizing the PL performance.[50] In the present system, the compound itself consists solely of organic cations and [MnBr$_4$]$^{2-}$. There are no dopant cations. However, a trend similar to concentration quenching is observed when combining our PLQY results with previous reports, as shown in Figure 5. The relationship between shortest Mn···Mn distances and PLQY is collated from the present study (red circles) and previous literature (blue squares). Although the PLQY is a quantifiable number, there is still uncertainty in the values reported due to experimental handling and errors.
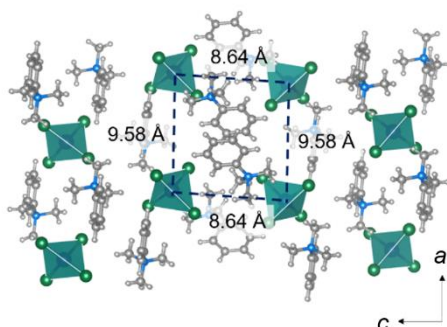
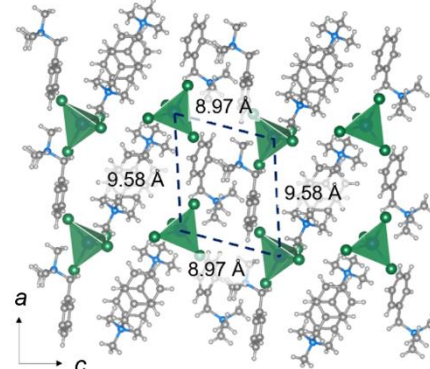**Figure 4.** (a) Organic *A* cation trimethylphenylammonium (TMPEA, left) and benzyltrimethylammonium (BTMA, right). (b) Crystal structure of (TMPEA)$_2$MnBr$_4$; Mn···Mn distances: 8.64 Å (shortest) and 9.58 Å labeled with blue dashes. (c) Crystal structure of (BTMA)$_2$MnBr$_4$, redrawn from ref. 41. Mn···Mn distances: 8.97 Å (shortest) and 9.58 Å labelled with blue dashes.

Table 1. Summary of (left) new and (right) reported $A_m MnBr_4$ (m = 1 or 2) (PRD = pyrrolidinium, ASN = 5-azonia-spiro[4,4]nonane, DIPA = diisopropylammonium, Bu$_4$N = tetrabutylammonium , PP14 = *N*-butyl-*N*-methylpiperidinium , P14 = *N*-butyl-*N*-methylpyrrolidinium), IPTMA = isopropyl-trimethylammonium, TEA = tetraethylammonium, TPA = tetrapropylammonium.*(P14)$_9$[Pb$_3$Br$_{11}$](MnBr$_4$)$_2$ is from ref. 51.

A (labelled in circles in Figure 5)	Space group	Shortest Mn-Mn distance (Å)	PLQY (%)	Lifetime (µs) 293K	*A* (reported, labelled in squares in Figure 5)	Space group	Shortest Mn-Mn distance (Å)	PLQY (%)	Lifetime (µs) 293K
DMA	$P2_1/n$	6.22, 6.85	7.8	81	P14[51]*	$P31c$	9.47, 9.48	50	114
3AMP	$P2_1$	6.52, 7.88	9.5	25	PRD2[52]	$P2_1/c$	8.03, 8.19	51	NA
3MP	$C2/m$	7.94, 7.97	13.0	19	IPTMA[53]	$Pnma$	8.52, 8.92	53	NA
HEP	$Pnma$	9.00, 9.00	25.5	49	PP14[43]	$C2/c$	9.43, 9.66	55	361
BTMA	$P2_1$	8.97, 9.18	51.1, 72[41]	236	DIPA[40]	$Iba2$	8.85, 9.06	62	1.44 ns
TMPEA	$C2/c$	8.64, 9.06	70.8, 98 (single crystal)	96	P14[43,54]	$P2_1/c$	8.84, 9.47	81	358
PRD[55]	$P2_1/n$	6.09, 6.30	16	0.73 ns	TEA[48]	$P\text{-}42_1m$	9.25, 9.26	79	NA
ASN[42]	$P2_12_12_1$	8.58, 9.24	13	NA	TPA[48]	$C2/c$	9.45, 10.29	89	NA
Bu$_4$N[44]	$P2_12_12_1$	8.95, 9.08	47	350	PPh$_4$[24]	$C2/c$	10.45, 11.38	98	NA

Thus, the trend in Figure 5 should be viewed as qualitative but not quantitative. From the new PLQY data reported here (five new compounds and one reported), we have found that the six of them (listed in Table 1, six in left half) have PLQYs varying from 7.8% [(DMA)$_2$MnBr$_4$] to 70.8% [(TMPEA)$_2$MnBr$_4$]. The single-crystal sample of (TMPEA)$_2$MnBr$_4$ has an even higher PLQY of 98% [Figure 6(b), insert]. In Figure 5, PLQY is increasing with increasing Mn···Mn distances. Depending on the crystal structure, there could be one or more tetrahedral Mn environments. Here we pick the two shortest Mn···Mn distances and obtain an averaged value to evaluate the level of separation of neighboring Mn ions. Detailed values are provided in Table 1. It is worth mentioning that, in previous reports, relatively high PLQY A_2MnBr$_4$ materials are all based on relatively bulky cations such as Bu$_4$N$^+$ or PPh$_4^+$, or smaller cations such as diisopropylammonium that achieved decent Mn···Mn separations (≈9 Å). In fact, most of the compounds with an average Mn···Mn distance of ~9 Å have high PLQYs (all above 10%). Crystal structures with larger Mn···Mn distances reduce energy transfer between Mn centers, originating from dipole−dipole interactions and symmetry-directed spin-exchange interactions.[26] The ones with the shortest Mn···Mn distances from 6-8 Å have generally lower PLQYs, where energy transfer occurs more easily over the shorter distances. Other factors that also play a part in determining the PLQY are: (i) The form of the sample (powder samples have lower than single crystals); ((ii) The rigidity of the system (rigid conjugated cations seem to more effectively prevent energy transfer); (iii) Interference from other components in the crystal structure. For example, our (HEP)$_3$MnBr$_5$ has relatively long Mn···Mn distances (9.00 and 9.00 Å, see Figure S1), but the presence of an extra Br$^-$ ions may have an influence on the PLQY. An similar example can be found in a previous report, where Li *et al.* reported two materials incorporating the same cation, *N*-butyl-*N*-methylpyrrolidinium (P14).[51,54] Although (P14)$_9$[Pb$_3$Br$_{11}$](MnBr$_4$)$_2$ has longer
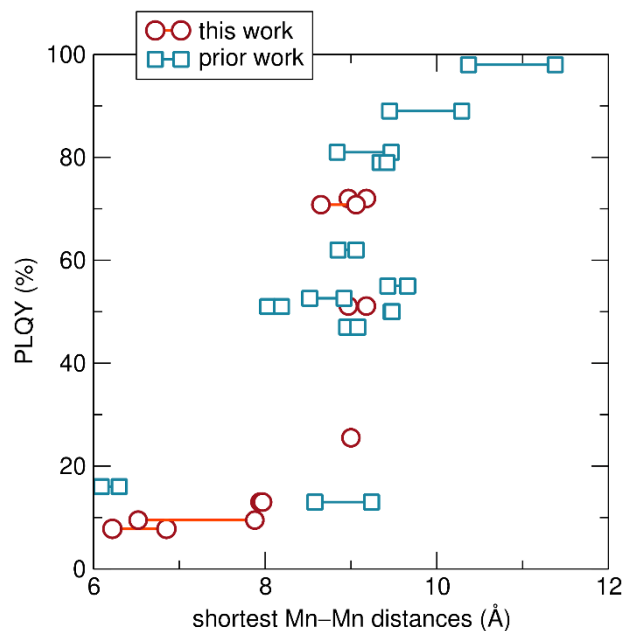

Figure 5. Correlation between shortest Mn···Mn distances and PLQY. Red circles represent the materials made and measured in this study (listed in Table 1, left columns). Blue squares are taken from the literature (listed in Table 1, right columns).
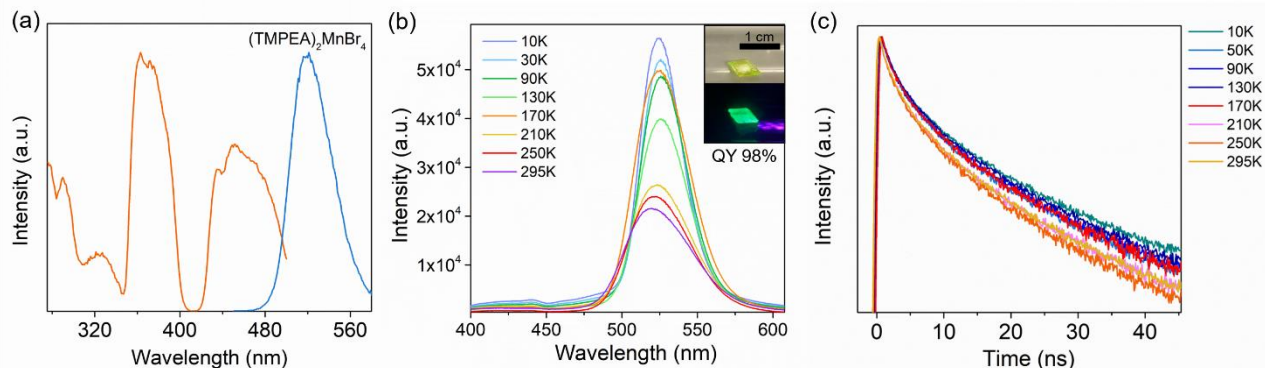
4

Figure 6. (a) Photoluminescence excitation (PLE) (orange) and emission (blue) spectra of $(TMPEA)_2MnBr_4$. (b) Temperature-dependent steady-state PL spectra of $(TMPEA)_2MnBr_4$. A single crystal of $(TMPEA)_2MnBr_4$ (PLQY 98%) is shown in the insert without and with irradiation under a UV flashlight (395 nm). (c) Temperature-dependent time-resolved PL decay spectra of $(TMPEA)_2MnBr_4$.

Mn⋯Mn distances than $(P14)_2MnBr_4$ (Table 1), the extra lead bromide units facilitate more energy transfer, leading to a lower PLQY (50% vs. 81%).

According to the Tanabe–Sugano diagram for high spin d^5 ions,[34] the excitation bands for A_mMnBr_4 (m = 1 or 2, A = DMA, 3AMP, 3MP, HEP, BTMA and TMPEA) could be assigned as shown in Table S18. The bands are mainly from two transitions: $^6A_1 \rightarrow {}^4G$ (430 – 490 nm) and $^6A_1 \rightarrow {}^4D$ (350 – 390 nm) (Figure 6a). All of the excitation band energies are similar in this group (see Figure 6a, S3) as the energies of the transitions are determined by the strength of the crystal-field splitting $\triangle$.[17,34] The PL emission originates from the radiative recombination from $^4T_1$ to $^6A_1$, and PL of all the compounds have about the same emission energy: TMPEA (2.38 eV, 520 nm), BTMA (2.39 eV, 519 nm), 3MP (2.37 eV, 523 nm), 3AMP (2.41 eV, 514 nm) and DMA (2.38 eV, 520 nm).

Temperature dependent PL and lifetime studies. We have chosen the compound with the highest PLQY, $(TMPEA)_2MnBr_4$, to study the temperature-dependent emission properties. With decreasing temperature, the intensity of the PL emission increases (Figure 6b), except the anomaly at 170K, which could be due to a phase transition related effect. A large single crystal was then picked out for PLQY measurement at room temperature; a PLQY value of 98% was recorded, which is much higher than the powdered sample (70.8%). Though high temperature measurements were not conducted, it is expected that the PL will be gradually quenched as the organic cations interact with $[MnBr_4]^{2-}$, leading to multiphonon (or multiroton) interactions.[34] The lifetimes of the PL decay for $(TMPEA)_2MnBr_4$ are gradually increasing with decreasing temperatures (Figure 6c). The room temperature lifetimes for the rest of the compound were provided in Table 1. The lifetimes vary from 16-236 μs, which are on the same scale of some previous reports.[43,44]

CONCLUSIONS

In conclusion, we have reported a series of new hybrid compounds with the general formula A_mMnBr_4 (A = DMA, 3AMP, 3MP, HEP and TMPEA, m = 1 or 2), which all exhibit green PL emission. Using single-crystal XRD for structural comparison and combining our results with previous literature reports, we identify a trend where the Mn⋯Mn distance is a highly dom-

inant factor for the PLQY in this class of materials. A high average Mn⋯Mn distance is beneficial for higher PLQY, due to a reduction in energy transfer processes between adjacent Mn centers. In effect, such structures reduce concentration quenching without the need to use dopant activator ions. Stoichiometric laser compounds that reduce energy transfer between rare-earth ions have been reported previously (e.g. NdP_5O_{14}), but we note that the Nd⋯Nd distances in such compounds are much smaller than can be achieved in the hybrid metal halides. A threshold, average Mn⋯Mn distance of ~9 Å guarantees a PLQY of at least 13% at room temperature in the present systems. To achieve greater separation of the $[MnBr_4]^{2-}$ ions in a hybrid system, a large, bulky and singly protonated cation is preferred to avoid intensive H-bonding interactions that pulls Mn tetrahedra closer together. One of the newly synthesized materials, $(TMPEA)_2MnBr_4$, has achieved a high PLQY of 70.8% for a powdered sample and 98% for a single-crystal sample, with an average shortest Mn⋯Mn distance of 8.9 Å. Our results highlight the structure-emission relationships in this important class of compounds and provide a design principle for the discovery of highly efficient, light-emitting materials.

METHODS

Materials. Manganese acetate (98%), dimethylamine hydrochloride (99%), 3-(aminomethyl)piperidine (Aldrich[CPR]), 3-methylpiperidine (99%), trimethylphenylammonium chloride (98%), benzyltrimethylammonium chloride (97%), heptamethylenimine (98%) and hydrobromic acid (ACS reagent, 48%) were purchased from Sigma-Aldrich and used as received.

Synthesis. The following procedure was used for synthesis of all the compounds. 5 mmol of manganese acetate (865 mg) was dissolved in 1.5 ml HBr, 10 mmol of A (A = dimethylamine hydrochloride, 3-(aminomethyl)piperidine and 3-methylpiperidine) was added directly to the previous mixture under heating and stirring until boiling. The solution was taken off the hotplate after the solution became clear and homogenous. Pale yellow crystals were formed under slow-cooling to room-temperature. For A = trimethylphenylammonium chloride, benzyltrimethylammonium chloride and heptamethylenimine, the amount of A cation was reduced by half using 5mmol instead due to the fast precipitation, and HBr was increased to 2 ml.

Single Crystal X-ray Diffraction. Full sphere data were collected using a Bruker KAPPA APEX II diffractometer equipped

with an APEX II CCD detector using a TRIUMPH monochromator with a Mo Kα source (λ = 0.71073 Å) with MX Optics or a Bruker D8 VENTURE diffractometer equipped with a Kappa goniometer stage, a PHOTON II CPAD detector and an IμS 3.0 Mo Kα source (λ = 0.71073 Å). Data were collected at 293K. The collected data were integrated and a multi-scan absorption correction was applied using the APEX2 software. Crystal structures were solved by direct methods (Full-matrix least-squares on F^2) using OLEX2 program.[56]

Steady-State and Time-Resolved Photoluminescence. Steady-state photoluminescent data were obtained using a Jovin HORIBA FluoroMax-4 (xenon source, 1 nm excitation and emission slit widths, 1 nm step size) equipped with a solid-state sample holder. Photoluminescent data were analyzed using the FluorEssence (v3.5) software powered by Origin. PLQY measurements were performed with a Quanta-φ integrating sphere (15 cm). All samples and the blank were excited at 360 nm (λ_{max}). Time-resolved PL spectra were captured with a streak camera (λ_{ex} = 340 nm). During the measurements, the samples were mounted in a vacuum cryostat and maintained under <10^{-7} Torr pressure.

ASSOCIATED CONTENT

X-ray crystallographic data (cif.), crystallographic details, powder X-ray diffraction (PXRD), additional photoluminescence (PL) data (pdf.) are available in the supporting information free of charge on the ACS Publications website.

AUTHOR INFORMATION

Corresponding Authors
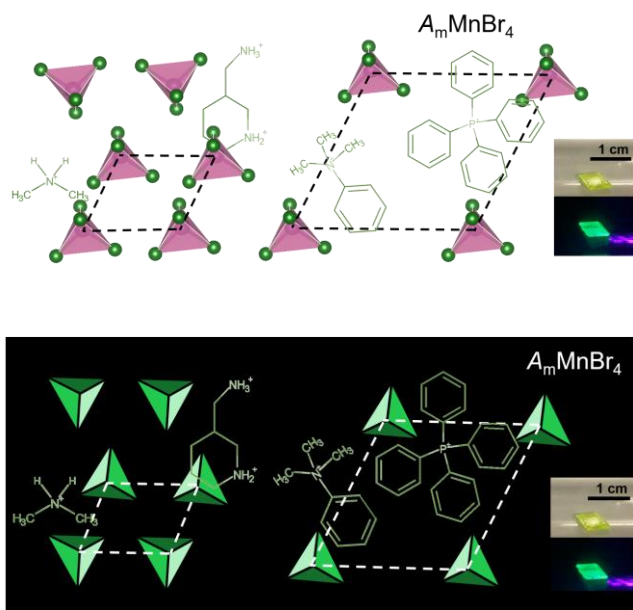* ramseshadri@ucsb.edu
* akc30@cam.ac.uk

ACKNOWLEDGMENT

REFERENCES

(1)   Kobayashi, H.; Cui, H.; Kobayashi, A. Organic Metals and Superconductors Based on BETS (BETS = Bis(ethylenedithio)tetraselenafulvalene). *Chem. Rev.* **2004**, *104*, 5265-5288.

(2)   Saparov, B.; Mitzi, D. B. Organic–Inorganic Perovskites: Structural Versatility for Functional Materials Design. *Chem. Rev.* **2016**, *116*, 4558-4596.

(3)   Gao, Y.; Shi, E.; Deng, S.; Shiring, S. B.; Snaider, J. M.; Liang, C.; Yuan, B.; Song, R.; Janke, S. M.; Liebman-Peláez, A.; Yoo, P.; Zeller, M.; Boudouris, B. W.; Liao, P.; Zhu, C.; Blum, V.; Yu, Y.; Savoie, B. M.; Huang, L.; Dou, L. Molecular engineering of organic–inorganic hybrid perovskites quantum wells. *Nat. Chem.* **2019**, *11*, 1151-1157.

(4)   Jeon, N. J.; Noh, J. H.; Yang, W. S.; Kim, Y. C.; Ryu, S.; Seo, J.; Seok, S. I. Compositional engineering of perovskite materials for high-performance solar cells. *Nature* **2015**, *517*, 476.

(5)   Saliba, M.; Matsui, T.; Domanski, K.; Seo, J.-Y.; Ummadisingu, A.; Zakeeruddin, S. M.; Correa-Baena, J.-P.; Tress, W. R.; Abate, A.; Hagfeldt, A.; Grätzel, M. Incorporation of rubidium cations into perovskite solar cells improves photovoltaic performance. *Science* **2016**, *354*, 206-209.

(6)   Stranks, S. D.; Snaith, H. J. Metal-halide perovskites for photovoltaic and light-emitting devices. *Nat. Nanotechnol.* **2015**, *10*, 391-402.

(7)   Cho, H.; Jeong, S.-H.; Park, M.-H.; Kim, Y.-H.; Wolf, C.; Lee, C.-L.; Heo, J. H.; Sadhanala, A.; Myoung, N.; Yoo, S.; Im, S. H.; Friend, R. H.; Lee, T.-W. Overcoming the electroluminescence efficiency limitations of perovskite light-emitting diodes. *Science* **2015**, *350*, 1222-1225.

(8)   Brenner, P.; Stulz, M.; Kapp, D.; Abzieher, T.; Paetzold, U. W.; Quintilla, A.; Howard, I. A.; Kalt, H.; Lemmer, U. Highly stable solution processed metal-halide perovskite lasers on nanoimprinted distributed feedback structures. *Appl. Phys. Lett.* **2016**, *109*, 141106.

(9)   Brenner, P.; Bar-On, O.; Jakoby, M.; Allegro, I.; Richards, B. S.; Paetzold, U. W.; Howard, I. A.; Scheuer, J.; Lemmer, U. Continuous wave amplified spontaneous emission in phase-stable lead halide perovskites. *Nat. Commun.* **2019**, *10*, 988.

(10)   Fang, Y.; Huang, J. Resolving Weak Light of Sub-picowatt per Square Centimeter by Hybrid Perovskite Photodetectors Enabled by Noise Reduction. *Adv. Mater.* **2015**, *27*, 2804-2810.

(11)   Fang, Y.; Dong, Q.; Shao, Y.; Yuan, Y.; Huang, J. Highly narrowband perovskite single-crystal photodetectors enabled by surface-charge recombination. *Nat. Photonics* **2015**, *9*, 679-686.

(12)   He, Y.; Matei, L.; Jung, H. J.; McCall, K. M.; Chen, M.; Stoumpos, C. C.; Liu, Z.; Peters, J. A.; Chung, D. Y.; Wessels, B. W.; Wasielewski, M. R.; Dravid, V. P.; Burger, A.; Kanatzidis, M. G. High spectral resolution of gamma-rays at room temperature by perovskite CsPbBr$_3$ single crystals. *Nat. Commun.* **2018**, *9*, 1609.

(13)   Stoumpos, C. C.; Malliakas, C. D.; Peters, J. A.; Liu, Z.; Sebastian, M.; Im, J.; Chasapis, T. C.; Wibowo, A. C.; Chung, D. Y.; Freeman, A. J.; Wessels, B. W.; Kanatzidis, M. G. Crystal Growth of the Perovskite Semiconductor CsPbBr$_3$: A New Material for High-Energy Radiation Detection. *Cryst. Growth Des.* **2013**, *13*, 2722-2727.

(14)   Mercier, N. Hybrid Halide Perovskites: Discussions on Terminology and Materials. *Angew. Chem. Int. Ed.* **2019**, *58*, 17912-17917.

(15)   Mao, L.; Guo, P.; Kepenekian, M.; Hadar, I.; Katan, C.; Even, J.; Schaller, R. D.; Stoumpos, C. C.; Kanatzidis, M. G. Structural Diversity in White-light Emitting Hybrid Lead Bromide Perovskites. *J. Am. Chem. Soc.* **2018**, *140*, 13078-13088.

(16)   Zhou, C.; Lin, H.; He, Q.; Xu, L.; Worku, M.; Chaaban, M.; Lee, S.; Shi, X.; Du, M.-H.; Ma, B. Low dimensional metal halide perovskites and hybrids. *Mat. Sci. Eng. R* **2019**, *137*, 38-65.

(17)   Morad, V.; Cherniukh, I.; Pöttschacher, L.; Shynkarenko, Y.; Yakunin, S.; Kovalenko, M. V. Manganese(II) in Tetrahedral Halide Environment: Factors Governing Bright Green Luminescence. *Chem. Mater.* **2019**, *31*, 10161-10169.

(18)   Lu, H.; Chamorro, J. R.; Wan, C.; McQueen, T. M. Universal Single-Ion Physics in Spin–Orbit-Coupled d5 and d4 Ions. *Inorg. Chem.* **2018**, *57*, 14443-14449.

(19)   Shilov, G. V.; Zhilyaeva, E. I.; Flakina, A. M.; Torunova, S. A.; Lyubovskii, R. B.; Aldoshin, S. M.; Lyubovskaya, R. N. Phase transition at 320 K in a new layered organic metal conductor (BEDT-TTF)$_4$CoBr$_4$(C$_6$H$_4$Cl$_2$). *CrystEngComm* **2011**, *13*, 1467-1473.

(20)   Chen, S.; Gao, J.; Chang, J.; Li, Y.; Huangfu, C.; Meng, H.; Wang, Y.; Xia, G.; Feng, L. Family of Highly Luminescent Pure Ionic Copper(I) Bromide Based Hybrid Materials. *ACS Appl. Mater. Interfaces* **2019**, *11*, 17513-17520.

(21)   Hua, X.-N.; Huang, C.-R.; Gao, J.-X.; Lu, Y.; Chen, X.-G.; Liao, W.-Q. High-temperature reversible phase transitions and exceptional dielectric anomalies in cobalt(ii) based ionic crystals: [Me$_3$NCH$_2$X]$_2$[CoX$_4$] (X = Cl and Br). *Dalton Trans.* **2018**, *47*, 6218-6224.

(22)   Liu, W.; Fang, Y.; Li, J. Copper Iodide Based Hybrid Phosphors for Energy-Efficient General Lighting Technologies. *Adv. Funct. Mater.* **2018**, *28*, 1705593.

(23)   Zhong, C.; Sasaki, T.; Jimbo-Kobayashi, A.; Fujiwara, E.; Kobayashi, A.; Tada, M.; Iwasawa, Y. Syntheses, structures, and properties of a series of metal ion-containing dialkylimidazolium ionic liquids. *Bull. Chem. Soc. Jpn* **2007**, *80*, 2365-2374.

(24)   Xu, L.-J.; Sun, C.-Z.; Xiao, H.; Wu, Y.; Chen, Z.-N. Green-Light-Emitting Diodes based on Tetrabromide Manganese(II) Complex through Solution Process. *Adv. Mater.* **2017**, *29*, 1605739.

(25)   Qin, Y.; Tao, P.; Gao, L.; She, P.; Liu, S.; Li, X.; Li, F.; Wang, H.; Zhao, Q.; Miao, Y.; Huang, W. Designing Highly Efficient Phosphorescent Neutral Tetrahedral Manganese(II) Complexes for Organic Light-Emitting Diodes. *Adv. Opt. Mater.* **2019**, *7*, 1801160.

(26)   Liu, Y.; Zhang, J.; Han, B.; Wang, X.; Wang, Z.; Xue, C.; Bian, G.; Hu, D.; Zhou, R.; Li, D.-S.; Wang, Z.; Ouyang, Z.; Li, M.; Wu, T. New Insights into Mn–Mn Coupling Interaction-Directed Photoluminescence Quenching Mechanism in Mn2+-Doped Semiconductors. *J. Am. Chem. Soc.* **2020**, *142*, 6649-6660.

(27)   Soo, Y. L.; Ming, Z. H.; Huang, S. W.; Kao, Y. H.; Bhargava, R. N.; Gallagher, D. Local structures around Mn luminescent centers in Mn-doped nanocrystals of ZnS. *Phys. Rev. B* **1994**, *50*, 7602-7607.

(28)   Chen, H.-Y.; Maiti, S.; Son, D. H. Doping Location-Dependent Energy Transfer Dynamics in Mn-Doped CdS/ZnS Nanocrystals. *ACS Nano* **2012**, *6*, 583-591.

(29)   Pradhan, N. Mn-Doped Semiconductor Nanocrystals: 25 Years and Beyond. *J. Phys. Chem. Lett.* **2019**, *10*, 2574-2577.

(30)   Majher, J. D.; Gray, M. B.; Strom, T. A.; Woodward, P. M. Cs$_2$NaBiCl$_6$:Mn^{2+}—A New Orange-Red Halide Double Perovskite Phosphor. *Chem. Mater.* **2019**, *31*, 1738-1744.

(31)   Locardi, F.; Cirignano, M.; Baranov, D.; Dang, Z.; Prato, M.; Drago, F.; Ferretti, M.; Pinchetti, V.; Fanciulli, M.; Brovelli, S.; De Trizio, L.; Manna, L. Colloidal Synthesis of Double Perovskite Cs$_2$AgInCl$_6$ and Mn-Doped Cs$_2$AgInCl$_6$ Nanocrystals. *J. Am. Chem. Soc.* **2018**, *140*, 12989-12995.

(32)   Ye, H.-Y.; Zhou, Q.; Niu, X.; Liao, W.-Q.; Fu, D.-W.; Zhang, Y.; You, Y.-M.; Wang, J.; Chen, Z.-N.; Xiong, R.-G. High-Temperature Ferroelectricity and Photoluminescence in a Hybrid Organic–Inorganic Compound: (3-Pyrrolinium)MnCl$_3$. *J. Am. Chem. Soc.* **2015**, *137*, 13148-13154.

(33)   Zhang, Y.; Liao, W.-Q.; Fu, D.-W.; Ye, H.-Y.; Chen, Z.-N.; Xiong, R.-G. Highly Efficient Red-Light Emission in An Organic–Inorganic Hybrid Ferroelectric: (Pyrrolidinium)MnCl3. *J. Am. Chem. Soc.* **2015**, *137*, 4928-4931.

(34)   Rodríguez-Lazcano, Y.; Nataf, L.; Rodríguez, F. Electronic structure and luminescence of [(CH$_3$)$_4$N]$_2$MnX$_4$ (X= Cl, Br) crystals at high pressures by time-resolved spectroscopy:

Pressure effects on the Mn-Mn exchange coupling. *Phys. Rev. B* **2009**, *80*, 085115.

(35)   Wei, Z.; Liao, W.-Q.; Tang, Y.-Y.; Li, P.-F.; Shi, P.-P.; Cai, H.; Xiong, R.-G. Discovery of an Antiperovskite Ferroelectric in [(CH$_3$)$_3$NH]$_3$(MnBr$_3$)(MnBr$_4$). *J. Am. Chem. Soc.* **2018**, *140*, 8110-8113.

(36)   Berezin, A. S.; Samsonenko, D. G.; Brel, V. K.; Artem'ev, A. V. "Two-in-one" organic–inorganic hybrid MnII complexes exhibiting dual-emissive phosphorescence. *Dalton Trans.* **2018**, *47*, 7306-7315.

(37)   Hardy, G. E.; Zink, J. I. Triboluminescence and pressure dependence of the photoluminescence of tetrahedral manganese(II) complexes. *Inorg. Chem.* **1976**, *15*, 3061-3065.

(38)   Cotton, F. A.; Daniels, L. M.; Huang, P. Correlation of Structure and Triboluminescence for Tetrahedral Manganese(II) Compounds. *Inorg. Chem.* **2001**, *40*, 3576-3578.

(39)   Barreda-Argüeso, J. A.; Nataf, L.; Rodríguez-Lazcano, Y.; Aguado, F.; González, J.; Valiente, R.; Rodríguez, F.; Wilhelm, H.; Jephcoat, A. P. Bulk and Molecular Compressibilities of Organic–Inorganic Hybrids [(CH$_3$)$_4$N]$_2$MnX$_4$ (X = Cl, Br); Role of Intermolecular Interactions. *Inorg. Chem.* **2014**, *53*, 10708-10715.

(40)   Jiang, C.; Zhong, N.; Luo, C.; Lin, H.; Zhang, Y.; Peng, H.; Duan, C.-G. (Diisopropylammonium)$_2$MnBr$_4$: a multifunctional ferroelectric with efficient green-emission and excellent gas sensing properties. *Chem. Comm.* **2017**, *53*, 5954-5957.

(41)   Cai, X.-W.; Zhao, Y.-Y.; Li, H.; Huang, C.-P.; Zhou, Z. Lead-free/rare earth-free Green-light-emitting crystal based on organic-inorganic hybrid [(C$_{10}$H$_{16}$N)$_2$][MnBr$_4$] with high emissive quantum yields and large crystal size. *J. Mol. Struct.* **2018**, *1161*, 262-266.

(42)   Xu, L.; Gao, J.-X.; Chen, X.-G.; Hua, X.-N.; Liao, W.-Q. A temperature-triggered triplex bistable switch in a hybrid multifunctional material: [(CH$_2$)$_4$N(CH$_2$)$_4$]$_2$[MnBr$_4$]. *Dalton Trans.* **2018**, *47*, 16995-17003.

(43)   Gong, L.-K.; Hu, Q.-Q.; Huang, F.-Q.; Zhang, Z.-Z.; Shen, N.-N.; Hu, B.; Song, Y.; Wang, Z.-P.; Du, K.-Z.; Huang, X.-Y. Efficient modulation of photoluminescence by hydrogen bonding interactions between inorganic [MnBr$_4$]$^{2-}$ anions and organic cations. *Chem. Comm.* **2019**, *55*, 7303-7306.

(44)   Jana, A.; Zhumagali, S.; Ba, Q.; Nissimagoudar, A. S.; Kim, K. S. Direct emission from quartet excited states triggered by upconversion phenomena in solid-phase synthesized fluorescent lead-free organic–inorganic hybrid compounds. *J. Mater. Chem. A* **2019**, *7*, 26504-26512.

(45)   Wei, Y.-L.; Jing, J.; Shi, C.; Ye, H.-Y.; Wang, Z.-X.; Zhang, Y. High quantum yield and unusual photoluminescence behaviour in tetrahedral manganese(ii) based on hybrid compounds. *Inorg. Chem. Front.* **2018**, *5*, 2615-2619.

(46)   Sen, A.; Swain, D.; Guru Row, T. N.; Sundaresan, A. Unprecedented 30 K hysteresis across switchable dielectric and magnetic properties in a bright luminescent organic–inorganic halide (CH$_6$N$_3$)$_2$MnCl$_4$. *J. Mater. Chem. C* **2019**, *7*, 4838-4845.

(47)   Fu, H.; Jiang, C.; Lao, J.; Luo, C.; Lin, H.; Peng, H.; Duan, C.-G. An organic–inorganic hybrid ferroelectric with strong luminescence and high Curie temperature. *CrystEngComm* **2020**, *22*, 1436-1441.

(48)   Chen, S.; Gao, J.; Chang, J.; Zhang, Y.; Feng, L. Organic-inorganic manganese (II) halide hybrids based paper sensor for the fluorometric determination of pesticide ferbam. *Sens. Actuators B Chem.* **2019**, *297*, 126701.

(49)   Hong, H. Y.-P. Crystal structures of neodymium metaphosphate (NdP$_3$O$_9$) and ultraphosphate (NdP$_5$O$_{14}$). *Acta Cryst. B* **1974**, *30*, 468-474.

(50)   Dexter, D. L.; Schulman, J. H. Theory of concentration quenching in inorganic phosphors. *J. Chem. Phys.* **1954**, *22*, 1063-1070.

(51)   Li, M.; Zhou, J.; Zhou, G.; Molokeev, M. S.; Zhao, J.; Morad, V.; Kovalenko, M. V.; Xia, Z. Hybrid Metal Halides with Multiple Photoluminescence Centers. *Angew. Chem. Int. Ed.* **2019**, *58*, 18670-18675.

(52)   Wu, Y.-X.; Wang, C.-F.; Li, H.-H.; Jiang, F.; Shi, C.; Ye, H.-Y.; Zhang, Y. Highly Efficient and Uncommon Photoluminescence Behavior Combined with Multiple Dielectric Response in Manganese(II) Based Hybrid Phase Transition Compounds. *Eur. J. Inorg. Chem.* **2020**, *2020*, 394-399.

(53)   Luo, Y.-Y.; Zhang, Z.-X.; Su, C.-Y.; Zhang, W.-Y.; Shi, P.-P.; Ye, Q.; Fu, D.-W. Tunable optoelectronic response multifunctional materials: exploring switching and photoluminescence integrated in flexible thin films/crystals. *J. Mater. Chem. C* **2020**, *8*, 7089-7095.

(54)   Li, M.; Zhou, J.; Molokeev, M. S.; Jiang, X.; Lin, Z.; Zhao, J.; Xia, Z. Lead-Free Hybrid Metal Halides with a Green-Emissive [MnBr$_4$] Unit as a Selective Turn-On Fluorescent Sensor for Acetone. *Inorg. Chem.* **2019**, *58*, 13464-13470.

(55)   Jiang, C.; Fu, H.; Han, Y.; Li, D.; Lin, H.; Li, B.; Meng, X.; Peng, H.; Chu, J. Tuning the Crystal Structure and Luminescence of Pyrrolidinium Manganese Halides via Halide Ions. *Cryst. Res. Technol.* **2019**, *54*, 1800236.

(56)   Dolomanov, O. V.; Bourhis, L. J.; Gildea, R. J.; Howard, J. A.; Puschmann, H. OLEX2: a complete structure solution, refinement and analysis program. *J. Appl. Crystallogr.* **2009**, *42*, 339-341.

TOC graphic

Design Principles for Enhancing Photoluminescence Quantum Yield in Hybrid Manganese Bromides

Lingling Mao[1], Peijun Guo[3,4], Shuxin Wang[1], Anthony K. Cheetham[1,5]* and

Ram Seshadri[1,2]*

[1]Materials Research Laboratory and Materials Department, [2]Department of Chemistry and Biochemistry, University of California, Santa Barbara, California 93106, United States

[3]Center for Nanoscale Materials, Argonne National Laboratory, 9700 South Cass Avenue, Lemont, Illinois 60439, United States

[4]Department of Chemical and Environmental Engineering, Yale University, 9 Hillhouse Avenue, New Haven, CT 06520, United States

[5]Department of Materials Science & Engineering, National University of Singapore 9 Engineering Drive 1, Singapore 117576, Singapore

Table of contents

Section S1. Crystallographic details.

Table S1. Crystal data and structure refinements for $(DMA)_2MnBr_4$, $(3AMP)MnBr_4 \cdot H_2O$ and $(3MP)_2MnBr_4$

Compound	$(DMA)_2MnBr_4$	$(3AMP)MnBr_4 \cdot H_2O$	$(3MP)_2MnBr_4$
formula	$(CH_3NH_2CH_3)_2MnBr_4$	$(C_6N_2H_{16})MnBr_4 \cdot H_2O$	$(C_6NH_{14})_2MnBr_4$
Temperature (K)	299.7	299.7	286.9
Crystal system	Monoclinic	Monoclinic	Monoclinic
Space group	$P2_1/n$	$P2_1$	$C2/m$
Unit cell dimensions	a = 8.2086(14) Å,	a = 8.481(8) Å,	a = 7.942(9) Å,
	b = 11.764(2) Å	b = 8.547(7) Å,	b = 13.820(16) Å,
	c = 15.237(3) Å	c = 10.645(9) Å	c = 19.45(2) Å
	$\beta = 95.147(5)°$	$\beta = 108.72(3)°$	$\beta = 101.59(3)°$
Volume ($Å^3$)	1465.5(4)	730.8(11)	2091(4)
Z	4	2	4
Density (g/cm^3)	2.116	2.312	1.827
Absorption coefficient	11.768 mm^{-1}	11.815 mm^{-1}	8.268 mm^{-1}
F(000)	876	482	1116
θ range for data collection	2.190 to 27.236 °	2.020 to 28.440 °	1.069 to 26.091 °
Index ranges	-10<=h<=10,	-11<=h<=5,	-9<=h<=9,
	-15<=k<=15,	-11<=k<=11,	-16<=k<=8,
	-16<=l<=19	-13<=l<=14	-23<=l<=22
Reflections collected	11303	5563	4437
Independent reflections	3241 [R_{int} = 0.0425]	3426 [R_{int} = 0.0488]	2798 [R_{int} = 0.0349]
Completeness to θ = 25.242°	99.7%	99.9%	98.5%
Refinement method	Full-matrix least-squares on F^2		
Data / restraints / parameters	3241 / 0 / 74	3426 / 1 / 131	2798 / 1 / 175
Goodness-of-fit	1.019	0.937	0.843
Final R indices [I > 2σ(I)]	R_{obs} = 0.0381,	R_{obs} = 0.0527,	R_{obs} = 0.0494,
	wR_{obs} = 0.0687	wR_{obs} = 0.1155	wR_{obs} = 0.1221
R indices [all data]	R_{all} = 0.0828,	R_{all} = 0.0745,	R_{all} = 0.0905,
	wR_{all} = 0.0799	wR_{all} = 0.1237	wR_{all} = 0.1454
Largest diff. peak and hole (e $Å^{-3}$)	0.712, -0.624	0.867, -1.191	0.591, -0.464

Table S2. Crystal data and structure refinements for $(TMPEA)_2MnBr_4$ and $(HEP)_3MnBr_4$.

Compound	$(TMPEA)_2MnBr_4$	$(HEP)_3MnBr_5$
formula	$(C_9NH_{14})_6Mn_3Br_{12}$	$(C_7H_{16}N)_3MnBr_5$
Temperature (K)	299.4	299.1
Crystal system	Monoclinic	Orthorhombic
Space group	$C2/c$	$Pnma$
Unit cell dimensions	a = 16.8875(14) Å, b = 9.0640(6) Å, c = 46.877(3) Å β = 92.765(4)°	a = 20.516(7) Å, b = 14.310(5) Å, c = 10.588(4) Å,
Volume (Å³)	7167.0(9)	3108.5(19)
Z	4	4
Density (g/cm³)	1.799	1.703
Absorption coefficient	7.247 mm^{-1}	6.865 mm^{-1}
F(000)	3780	1580
θ range for data collection	0.870 to 26.094°	1.985 to 28.011°
Index ranges	-13<=h<=19, -10<=k<=11, -57<=l<=57	-25<=h<=26, -17<=k<=17, -13<=l<=9
Reflections collected	13994	20695
Independent reflections	3553 [R_{int} = 0.0380]	3553 [R_{int} = 0.0380]
Completeness to θ = 25.242°	97.3%	100%
Refinement method	Full-matrix least-squares on F²	
Data / restraints / parameters	6867 / 4 / 333	3553 / 11 / 81
Goodness-of-fit	1.045	1.055
Final R indices [I > 2σ(I)]	R_{obs} = 0.0897, wR_{obs} = 0.2785	R_{obs} = 0.0727, wR_{obs} = 0.2130
R indices [all data]	R_{all} = 0.1437, wR_{all} = 0.3200	R_{all} = 0.1373, wR_{all} = 0.2593
Largest diff. peak and hole (e·Å^{-3})	2.904 and -1.363	2.770 and -1.018

Table S3. Anisotropic displacement parameters ($Å^2 \times 10^3$) for $(DMA)_2MnBr_4$ with estimated standard deviations in parentheses.

Label	U_{11}	U_{22}	U_{33}	U_{12}	U_{13}	U_{23}
Br(1)	54(1)	50(1)	67(1)	-3(1)	-13(1)	-7(1)
Br(2)	64(1)	40(1)	67(1)	-3(1)	7(1)	6(1)
Br(3)	65(1)	53(1)	48(1)	-3(1)	2(1)	9(1)
Br(4)	49(1)	70(1)	84(1)	12(1)	17(1)	-10(1)
Mn(5)	38(1)	39(1)	46(1)	2(1)	3(1)	0(1)

The anisotropic displacement factor exponent takes the form: $-2\pi^2[h^2a^{*2}U_{11} + ... + 2hka^*b^*U_{12}]$.

Table S4. Selected bond lengths [Å] for $(DMA)_2MnBr_4$ with estimated standard deviations in parentheses.

Label	Distances
Br(1)-Mn(5)	2.5013(10)
Br(2)-Mn(5)	2.4961(9)
Br(3)-Mn(5)	2.5202(10)
Br(4)-Mn(5)	2.4812(9)

Symmetry transformations used to generate equivalent atoms:

Table S5. Selected bond angles [°] for $(DMA)_2MnBr_4$ with estimated standard deviations in parentheses.

Label	Angles
Br(1)-Mn(5)-Br(3)	105.09(3)
Br(2)-Mn(5)-Br(1)	109.18(3)
Br(2)-Mn(5)-Br(3)	110.11(3)
Br(4)-Mn(5)-Br(1)	111.04(4)
Br(4)-Mn(5)-Br(2)	111.99(3)
Br(4)-Mn(5)-Br(3)	109.22(3)

Symmetry transformations used to generate equivalent atoms:

Table S6. Anisotropic displacement parameters ($\text{Å}^2 \times 10^3$) for (3AMP)MnBr$_4$·H$_2$O with estimated standard deviations in parentheses.

Label	U_{11}	U_{22}	U_{33}	U_{12}	U_{13}	U_{23}
Br(01)	41(1)	29(1)	36(1)	-3(1)	16(1)	-4(1)
Br(02)	32(1)	28(1)	55(1)	-4(1)	23(1)	-4(1)
Br(03)	28(1)	30(1)	56(1)	2(1)	18(1)	-6(1)
Br(04)	50(1)	34(1)	34(1)	13(1)	15(1)	7(1)
Mn(05)	26(1)	25(2)	35(2)	2(1)	13(1)	4(1)

The anisotropic displacement factor exponent takes the form: $-2\pi^2[h^2 a^{*2} U_{11} + \ldots + 2hka^* b^* U_{12}]$.

Table S7. Selected bond lengths [Å] for (3AMP)MnBr$_4$·H$_2$O with estimated standard deviations in parentheses.

Label	Distances
Br(01)-Mn(05)	2.528(3)
Br(02)-Mn(05)	2.491(3)
Br(03)-Mn(05)	2.500(3)
Br(04)-Mn(05)	2.495(3)

Symmetry transformations used to generate equivalent atoms:

Table S8. Selected bond angles [°] for (3AMP)MnBr$_4$·H$_2$O with estimated standard deviations in parentheses.

Label	Angles
Br(02)-Mn(05)-Br(01)	108.55(10)
Br(02)-Mn(05)-Br(03)	115.86(11)
Br(02)-Mn(05)-Br(04)	113.01(9)
Br(03)-Mn(05)-Br(01)	102.74(9)
Br(04)-Mn(05)-Br(01)	106.63(11)
Br(04)-Mn(05)-Br(03)	109.17(10)

Symmetry transformations used to generate equivalent atoms:

Table S9. Anisotropic displacement parameters ($Å^2$x10^3) for $(3MP)_2MnBr_4$ with estimated standard deviations in parentheses.

Label	U_{11}	U_{22}	U_{33}	U_{12}	U_{13}	U_{23}
Br(2)	48(1)	50(2)	71(2)	6(1)	0(1)	5(1)
Br(3)	68(2)	48(2)	78(2)	13(1)	27(1)	0(1)
Br	57(1)	57(2)	74(2)	5(1)	27(1)	-6(1)
Br(1)	61(2)	54(2)	75(2)	16(1)	1(1)	0(1)
Mn(1)	45(2)	27(2)	67(2)	0	12(2)	0
Mn	45(2)	38(2)	65(2)	0	15(2)	0

The anisotropic displacement factor exponent takes the form: $-2\pi^2[h^2a^{*2}U_{11} + ... + 2hka^*b^*U_{12}]$.

Table S10. Selected bond lengths [Å] for $(3MP)_2MnBr_4$ with estimated standard deviations in parentheses.

Label	Distances
Br(2)-Mn(1)	2.500(3)
Br(3)-Mn(1)	2.503(3)
Br-Mn	2.499(3)
Br(1)-Mn	2.505(3)

Symmetry transformations used to generate equivalent atoms:

(1) -x+1,y,-z+1 (2) -x+1,y,-z+2

Table S11. Selected bond angles [°] for $(3MP)_2MnBr_4$ with estimated standard deviations in parentheses.

Label	Angles
Br(2)-Mn(1)-Br(2)#1	104.69(18)
Br(2)#1-Mn(1)-Br(3)#1	109.18(10)
Br(2)-Mn(1)-Br(3)	109.18(10)
Br(2)-Mn(1)-Br(3)#1	112.66(10)
Br(2)#1-Mn(1)-Br(3)	112.66(10)
Br(3)#1-Mn(1)-Br(3)	108.49(17)
Br-Mn-Br#2	104.37(19)
Br#2-Mn-Br(1)#2	109.15(10)
Br#2-Mn-Br(1)	112.73(9)
Br-Mn-Br(1)	109.15(10)

Br-Mn-Br(1)#2	112.73(9)
Br(1)-Mn-Br(1)#2	108.74(19)

Symmetry transformations used to generate equivalent atoms:

(1) -x+1,y,-z+1 (2) -x+1,y,-z+2

Table S12. Anisotropic displacement parameters ($\text{Å}^2 \times 10^3$) for $(HEP)_3MnBr_5$ with estimated standard deviations in parentheses.

Label	U_{11}	U_{22}	U_{33}	U_{12}	U_{13}	U_{23}
Br(01)	63(1)	61(1)	60(1)	0	-9(1)	0
Br(02)	70(1)	61(1)	66(1)	13(1)	-1(1)	-5(1)
Br(03)	64(1)	94(2)	64(1)	0	17(1)	0
Br(04)	83(2)	83(2)	68(1)	0	-22(1)	0
Mn(05)	53(2)	52(2)	49(2)	0	2(1)	0

The anisotropic displacement factor exponent takes the form: $-2\pi^2[h^2a^{*2}U_{11} + ... + 2hka^*b^*U_{12}]$.

Table S13. Selected bond lengths [Å] for $(HEP)_3MnBr_5$ with estimated standard deviations in parentheses.

Label	Distances
Br(02)-Mn(05)	2.5101(17)
Br(03)-Mn(05)	2.515(3)
Br(04)-Mn(05)	2.469(3)
Mn(05)-Br(02)#1	2.5101(17)

Symmetry transformations used to generate equivalent atoms:

(1) x,-y+3/2,z

Table S14. Selected bond angles [°] for $(HEP)_3MnBr_5$ with estimated standard deviations in parentheses.

Label	Angles
Br(02)-Mn(05)-Br(02)#1	106.63(9)
Br(02)#1-Mn(05)-Br(03)	106.62(6)
Br(02)-Mn(05)-Br(03)	106.62(6)
Br(04)-Mn(05)-Br(02)	111.95(6)
Br(04)-Mn(05)-Br(02)#1	111.95(6)

Br(04)-Mn(05)-Br(03)	112.65(10)

Symmetry transformations used to generate equivalent atoms:

(1) x,-y+3/2,z

Table S15. Anisotropic displacement parameters ($\text{Å}^2 \times 10^3$) for $(TMPEA)_2MnBr_4$ with estimated standard deviations in parentheses.

Label	U_{11}	U_{22}	U_{33}	U_{12}	U_{13}	U_{23}
Br(03)	70(1)	54(1)	70(1)	-11(1)	3(1)	0
Br(04)	67(1)	63(1)	77(2)	-8(1)	4(1)	2(1)
Mn(01)	26(2)	22(2)	29(2)	0	16(1)	-3(1)
Br(05)	68(2)	73(2)	70(2)	-9(1)	-13(1)	-10(1)
Br(06)	89(2)	58(1)	76(2)	15(1)	-5(1)	-3(1)
Br(07)	85(2)	79(2)	62(1)	-17(1)	22(1)	0(1)
Br(08)	91(2)	63(2)	104(2)	28(1)	8(1)	4(1)
Mn(02)	35(1)	23(1)	30(1)	4(1)	11(2)	18(1)

The anisotropic displacement factor exponent takes the form: $-2\pi^2[h^2a^{*2}U_{11} + \ldots + 2hka^*b^*U_{12}]$.

Table S16. Bond lengths [Å] for $(TMPEA)_2MnBr_4$ with estimated standard deviations in parentheses.

Label	Distances
Br(03)-Mn(01)	2.4602(19)
Br(04)-Mn(01)	2.4470(19)
Mn(01)-Br(03)#1	2.4601(19)
Mn(01)-Br(04)#1	2.4470(19)
Br(05)-Mn(02)	2.451(2)
Br(06)-Mn(02)	2.430(2)
Br(07)-Mn(02)	2.457(2)
Br(08)-Mn(02)	2.438(2)

Symmetry transformations used to generate equivalent atoms:

(1) -x+2,y,-z+3/2

Table S17. Selected bond angles [°] for (TMPEA)$_2$MnBr$_4$ with estimated standard deviations in parentheses.

Label	Angles
Br(03)#1-Mn(01)-Br(03)	102.77(10)
Br(04)#1-Mn(01)-Br(03)	114.59(6)
Br(04)#1-Mn(01)-Br(03)#1	108.63(6)
Br(04)-Mn(01)-Br(03)#1	114.59(6)
Br(04)-Mn(01)-Br(03)	108.63(6)
Br(04)#1-Mn(01)-Br(04)	107.79(11)
Br(05)-Mn(02)-Br(07)	107.60(8)
Br(06)-Mn(02)-Br(05)	109.44(9)
Br(06)-Mn(02)-Br(07)	107.08(8)
Br(06)-Mn(02)-Br(08)	108.80(9)
Br(08)-Mn(02)-Br(05)	110.02(9)
Br(08)-Mn(02)-Br(07)	113.80(9)

Symmetry transformations used to generate equivalent atoms:

(1) -x+2,y,-z+3/2
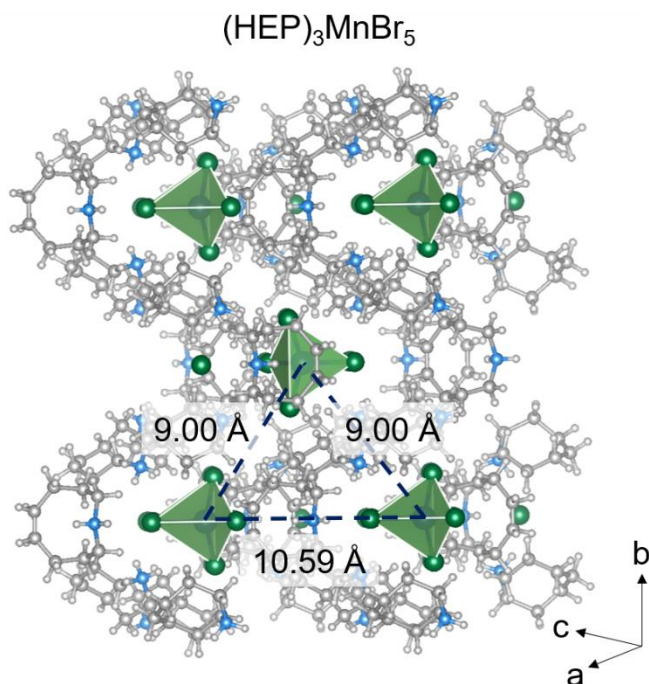
Figure S1. Crystal structure of (HEP)$_3$MnBr$_5$. Isolated Br$^-$ anions are present in the structure due to H-bondings with the organic cations.

Section S2. Calculated and experimental PXRD.
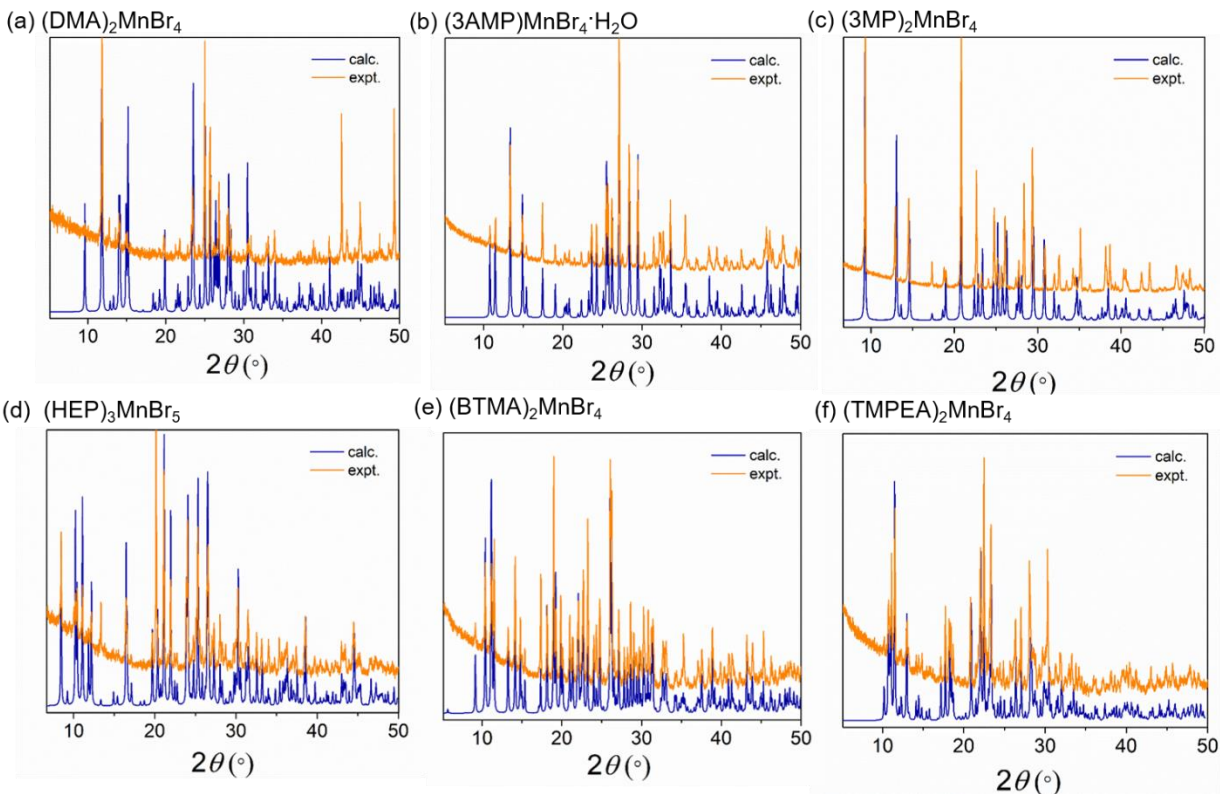
Figure S2. Calculated and experimental powder X-ray diffraction patterns of (a) $(DMA)_2MnBr_4$, (b) $(3AMP)MnBr_4 \cdot H_2O$, (c) $(3MP)_2MnBr_4$, (d) $(HEP)_3MnBr_5$, (e) $(BTMA)_2MnBr_4$ and (f) $(TMPEA)_2MnBr_4$.

Table S18. Assignment of experimental transition energies for $(TMPEA)_2MnBr_4$.

Excitation band	Energy (eV)	Excitation band	Energy (eV)
$^6A_1(S) \rightarrow {}^4T_1(G)$	2.64 (470 nm)	$^6A_1(S) \rightarrow {}^4T_1(P)$	3.83 (324 nm)
$\rightarrow {}^4T_2(G)$	2.74 (452 nm)	$\rightarrow {}^4A_2(F)$	4.29 (289 nm)
$\rightarrow {}^4A_1, \ {}^4E(G)$	2.84 (436 nm)	$\rightarrow {}^4T_1(F)$	4.49 (276 nm)
$\rightarrow {}^4T_2(D)$	3.34 (371 nm)	Emission $^4T_1 \rightarrow {}^6A_1$	2.38 (520 nm)
$\rightarrow {}^4E(D)$	3.42 (363 nm)	Stokes shift $^4T_1 \leftrightarrow {}^6A_1$	0.26

Section S3. Additional PL data.
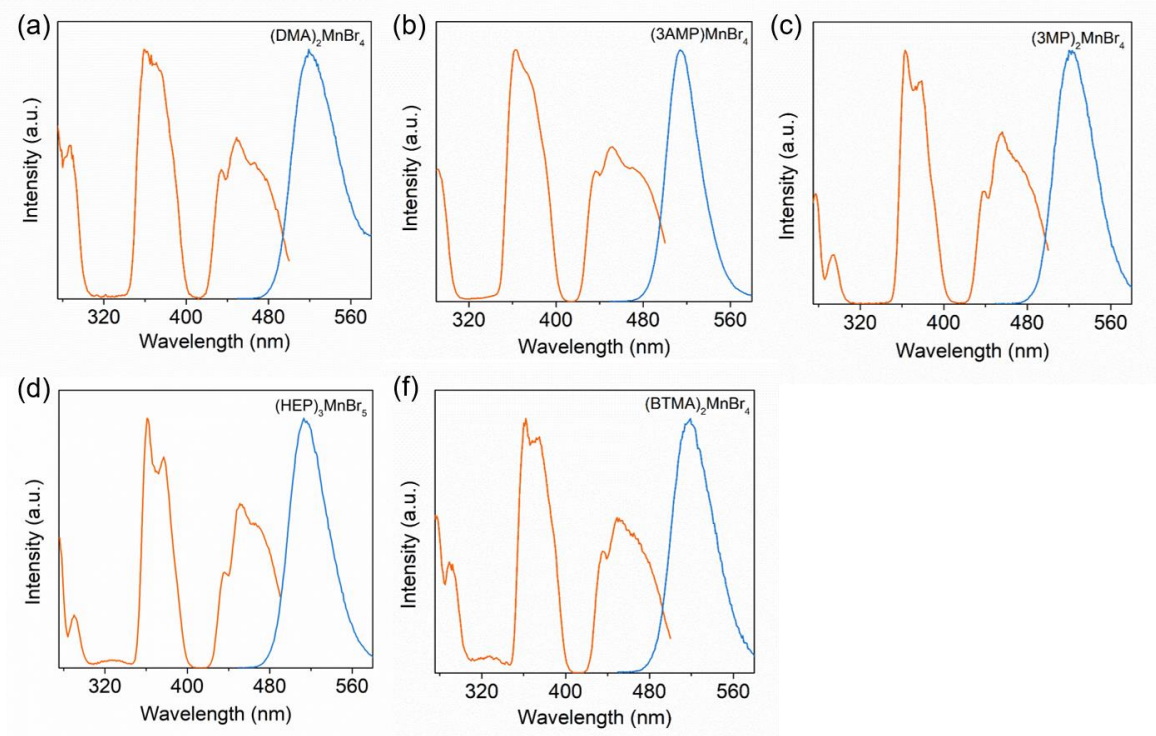
Figure S3. PLE (orange) and PL (blue) spectra of (a) $(DMA)_2MnBr_4$, (b) $(3AMP)MnBr_4 \cdot H_2O$, (c) $(3MP)_2MnBr_4$, (d) $(HEP)_3MnBr_5$ and (e) $(BTMA)_2MnBr_4$.
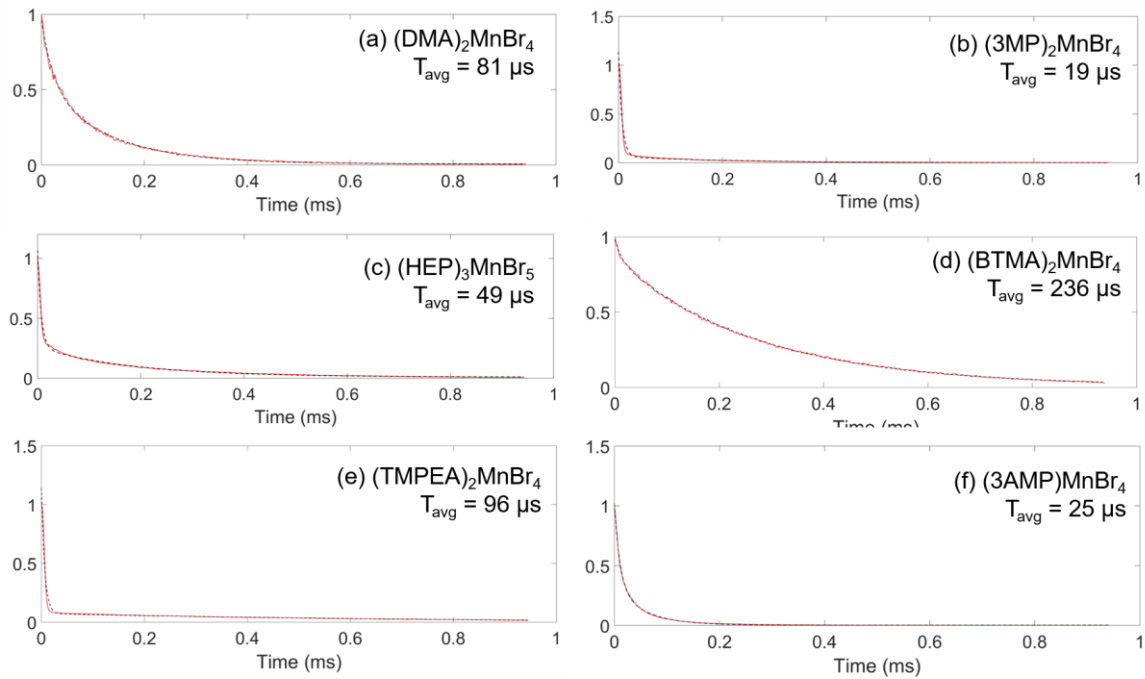
Figure S4. Time-resolved PL decay of (a) $(DMA)_2MnBr_4$, (b) $(3MP)_2MnBr_4$, (c) $(HEP)_3MnBr_5$, (d) $(BTMA)_2MnBr_4$, (e) $(TMPEA)_2MnBr_4$ and (f) $(3AMP)MnBr_4 \cdot H_2O$.
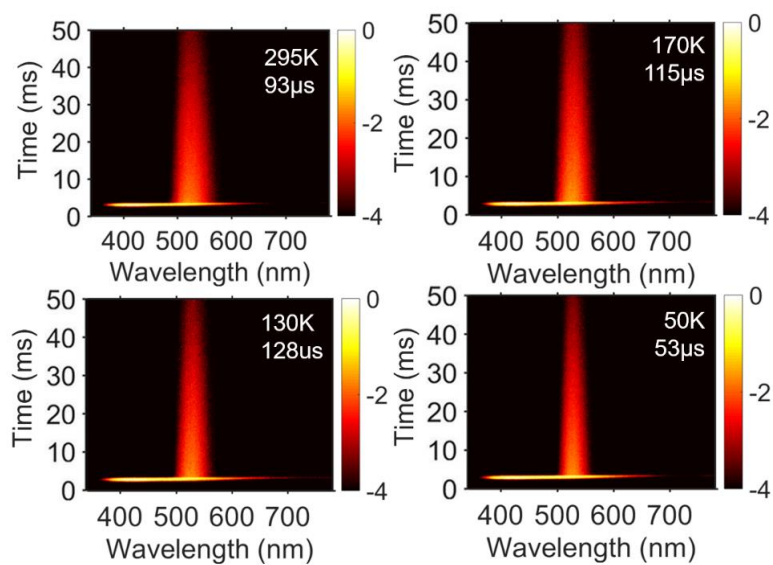
Figure S5. 2D time-resolved PL spectra of (TMPEA)$_2$MnBr$_4$ at selected temperatures. Averaged PL lifetimes are given on the right top corner of each spectrum.